

# First Principles Insights into Amorphous Mg<sub>2</sub>Sn Alloy Anode for Mg-ion Batteries

Majid Mortazavi,<sup>\*,†,‡</sup> Edmund Soon,<sup>†</sup> and Nikhil V. Medhekar<sup>†</sup>

<sup>†</sup>*Department of Materials Engineering, Monash University, Clayton, Victoria 3800, Australia*

<sup>‡</sup>*Fritz-Haber-Institut der Max-Planck-Gesellschaft, Faradayweg 4-6, 14195 Berlin, Germany*

E-mail: maj.mortazavi@gmail.com

## Abstract

Rechargeable Mg-ion batteries (MIBs) are an advantageous alternative solution to Li-ion batteries in many ways. Mg is safer and abundant in the Earth, and has a high electrochemical capacity owing to its divalent nature. It is yet relatively less studied largely due to primal success of Li-base batteries and challenges associated with the design of MIBs including high performance electrode materials. Herein, using first-principles calculation, we study the electrochemical and mechanical properties of the most viable alloy anode Mg<sub>2</sub>Sn with special attention to its amorphous phase—unavoidable phase forming during cyclic Sn magnesiation in MIBs due to volume changes. We create amorphous Mg<sub>2</sub>Sn via simulated annealing technique using *ab initio* molecular dynamics. We find while Mg<sub>2</sub>Sn undergoes a substantial atomic-level structural changes during the crystal-to-amorphous transformation, its polycrystalline properties degrade slightly and become softer by only 20% compared to the crystal phase. Moreover, we predict competitive electrochemical properties for the amorphous phase assuming it goes under similar reaction path as the average electronic charge on Mg ions almost remain unaffected. This work thus not only demonstrate that a-Mg<sub>2</sub>Sn

phase could be a bypass to combat the challenges associated with the crystal cracking during volume change, but also serves as first step to better understand the widely used  $\text{Mg}_2\text{Sn}$  alloy anode in MIBs.

## Introduction

Li-ion batteries (LIBs) are considered the most important and widespread energy storage solution in consumer electronics largely owing to their unrivaled combination of high volumetric and gravimetric energy capacities, and indeed their early technological maturity in 1991.<sup>1,2</sup> They are also seen as an immediate viable candidate for the next generation of electric vehicles reducing our dependence on fossil fuels.<sup>3</sup> The ever-increasing reliance on limited Li reserves as well as inherent safety issues and environmental impacts associated with LIBs, however, have raised concerns about the sustainability of this technology.<sup>4</sup> Na-ion batteries (NIBs) have emerged an appealing alternative solution with multifaceted benefits such as less expensive sodium precursors, and being more abundant and less toxic.<sup>5</sup> The performance of NIBs have constantly being improved especially during the last few years.<sup>5,6</sup> Yet this relatively unexplored technology is far behind its Li-counterparts limiting its application due to its intrinsic differences, and debated cost advantage.<sup>5,7</sup> Still they are deemed as an ideal storage technology for large-scale applications i.e. power grids, where size is not a major design concern.<sup>2,5,8</sup> The situation has fueled an active research towards the development of alternative safe and cost-effective technologies beyond LIBs technology.<sup>9-12</sup>

Mg-ion batteries (MIBs) are further recognized as attractive low-cost and high-capacity substitute for energy storage. Mg is naturally abundant in the Earth and is environmentally benign, and has a negative reduction potential of -2.37 V vs. SHE. The divalency of  $\text{Mg}^{2+}$  cations gives an attractive volumetric energy density in excess of  $3833 \text{ mAh ml}^{-1}$ , approximately twofold(threefold) higher than Li(Na). In addition, MIBs offer wider operating temperatures and better safety features compared to LIBs due to higher melting temperature of Mg ( $648.8^\circ\text{C}$ ). The formation of a passivation layer at the interface of electrode and elec-

trolyte during Mg plating and stripping completely blocking  $\text{Mg}^{2+}$  ions to shuttle, and the strong electrostatic interaction of  $\text{Mg}^{2+}$  with the host largely hampering  $\text{Mg}^{2+}$  ions mobility are major drawbacks hindering their practical applications. Addressing these issues have become the mainstream of MIBs' research and development.<sup>13-15</sup> There has been a promising progress on finding compatible electrolytes and suitable electrodes led to the introduction of promising electrolytes and cathode candidates.<sup>16-20</sup> However, identifying failure-free anode materials has received less attention and remains a big challenge.

The dendrite-free Mg metal initially gained popularity as an anode material for MIBs. It was later realized that its application is largely impeded due to the formation of the reduced layer.<sup>13,21</sup> Magnesium alloys, a family of insertion-type materials based on Mg alloying/de-alloying, are then found the most appealing anode candidates owing to their superior volumetric and gravimetric capacities as well as their compatibility with conventional electrolytes (e.g. magnesium salts).<sup>22-25</sup> The magnesianation of group-14,15 elements during the electrochemical reaction was reported experimentally.<sup>26-35</sup> It was shown that Sn could achieve higher gravimetric capacities than other group-14,15 elements, and operates in a low voltage window.<sup>28,32-37</sup> Moreover, some theoretical studies suggest that Sn ( $\alpha/\beta$ -Sn) is the most competitive alloy anode for MIBs due to relatively low diffusion barriers of Mg ions.<sup>27,35,38</sup>

Nevertheless, Sn magnesianation results in large structural changes in an electrochemical cell—in excess of 180 % volume change with reference to pure Sn during the formation of crystalline  $\text{Mg}_2\text{Sn}$  (c- $\text{Mg}_2\text{Sn}$ ).<sup>27-29</sup> It is well established that the electrochemical performance of alloys is largely hampered by structural failures as a result of drastic volume changes upon successive intercalation and de-intercalation of active ions during charge and discharge.<sup>13,39-42</sup> Sn magnesianation during charge and discharge results in remarkable capacity fade.<sup>36</sup> The underlying reasons are not clear, it is hypothesized that, along with the known issue of the formation of the passivation layer, large structural changes accompanied by pulverization and amorphization could be responsible.<sup>28,36</sup> Very recent strategies like the formation of nanostructured Sn<sup>34</sup> or dual phase alloying of nanoporous Bi-Sn alloy<sup>25</sup> or developing eutectic

alloys have demonstrated a very good progress; still remains an open challenge in the field. Sn magnesianation is somewhat similar but less severe to alloy anodes in LIBs and NIBs in terms of expansion; there is a crucial difference though. In Li/Na-based alloy anodes, various crystalline and amorphous phases coexist during charge and discharge complicates the phase transformations leading to the accumulation of internal stresses due to the coherent boundaries between phases.<sup>43-47</sup> For Mg-Sn system,  $\text{Mg}_2\text{Sn}$  is the only binary equilibria phase, hence less susceptible to detrimental phase transformations.<sup>48,49</sup> Yet Sn magnesianation causing drastic volume changes lead to the inevitable magnesianation-induced amorphization affecting the electrode performance.<sup>36</sup> Understanding the mechanical behavior during charge and discharge is essentially the first step towards designing a failure-free electrode.<sup>50-52</sup> While c- $\text{Mg}_2\text{Sn}$  is studied extensively in literature,<sup>53-56</sup> to the best of our knowledge, no information is available about the atomic structure as well as mechanical properties of electrochemically formed amorphous  $\text{Mg}_2\text{Sn}$  phase (a- $\text{Mg}_2\text{Sn}$ ). These properties are well documented for Li and Na binary alloys, whereas such knowledge is missing for the Mg-Sn system.<sup>43-47</sup>

In this work, we study the fundamental electrochemical and elastic properties of  $\text{Mg}_2\text{Sn}$ —the only phase in the binary Mg-Sn system at equilibrium—in crystalline and amorphous form using first principles calculations.<sup>48,49</sup> We obtained the atomic level structure of a- $\text{Mg}_2\text{Sn}$  by creating an amorphous phase using simulated annealing technique at three temperatures (above the melting point of c- $\text{Mg}_2\text{Sn}$  phase) using *ab initio* molecular dynamics. We provide a quantitative and qualitative atomic level insight into the a- $\text{Mg}_2\text{Sn}$  phase using radial distribution functions and rings statistics. Our results suggest that a- $\text{Mg}_2\text{Sn}$  is elastically softer than c- $\text{Mg}_2\text{Sn}$ , and it is alike c- $\text{Mg}_2\text{Sn}$  in terms of electrochemical properties.

## Methodology

The Vienna Ab Initio Simulation Package (VASP) was used to perform density functional theory (DFT) calculations within GGA-PBE approximation.<sup>57</sup> Projector-augmented wave

Table 1: Optimized lattice parameters (a, b, and c in Å) and formation energy  $E_f$  (in eV) of Mg, c-Mg<sub>2</sub>Sn,  $\beta$ -Sn, and a-Mg<sub>2</sub>Sn obtained from our DFT calculations.

Phase	x	Space Group	a	b	c	$E_f$
crystalline						
$\beta$ -Sn	0.00	I4 <sub>1</sub> /amd	5.95	5.95	3.21	-
Mg <sub>2</sub> Sn	2.0	Fm $\bar{3}$ m	6.82	6.82	6.82	-0.192
Mg	0.00	P6 <sub>3</sub> /mmc	3.20	3.20	5.18	-
amorphous						
Mg <sub>2</sub> Sn*	2.0	-	6.52	6.71	6.82	-0.064

\* The corresponding unit cell of the used a-Mg<sub>2</sub>Sn super cell.

(PAW) pseudopotentials were employed for describing core and valence electrons interactions.<sup>58,59</sup> The  $2p^63s^2$  and  $4d^{10}5s^25p^2$  states were treated as valence electrons for Mg and Sn, respectively. All crystalline phases were obtained from the crystal structure database.<sup>60</sup> For geometry optimization we used a  $7\times 7\times 7$  Monkhorst-Pack k-point sampling for the unit cell of c-Mg<sub>2</sub>Sn and a plane-wave kinetic energy cutoff of 500 eV ensuring the total energy converge within 1 meV/atom.<sup>61</sup> The structures were then optimized by allowing lattice vectors and ionic positions to relax until the Hellmann-Feynman forces were less than 0.01 eV/Å. A denser k-point ( $15\times 15\times 15$  grid) and higher energy cutoff (700 eV) were used for the same cell for the single-point energy calculations.

We used a  $2\times 2\times 2$  super cell of c-Mg<sub>2</sub>Sn to create the a-Mg<sub>2</sub>Sn phase. Using *ab initio* molecular dynamics (AIMD) as implemented in VASP, the structure was annealed up to three different temperatures (1600 K, 1800 K, 2000 K) above the melting point of c-Mg<sub>2</sub>Sn (1053 K). These tests allow to examine the impact of annealing temperature on amorphousity. The temperature was then maintained for 1000 MD time steps (time step = 2 fs). The system was then quenched rapidly down to room temperature at the rate of  $20\times 10^{14}$ K/s. Finally the system was allowed to equilibrate at this temperature for another 2500 MD time steps for (time step = 2 fs). We analyzed the produced a-Mg<sub>2</sub>Sn phases using radial distribution functions (RDFs) and rings statistics as implemented in Interactive Structure Analysis of Amorphous and Crystalline Systems (I.S.A.A.C.S) software package.<sup>62</sup>

The a-Mg<sub>2</sub>Sn structure was relaxed with a similar plane wave kinetic energy cutoff and

an atomic force tolerance of 0.02 eV/Å, and a  $7 \times 7 \times 7$  k-point Monkhorst-Pack grid. We then calculated the formation energy  $E_f$  with respect to Mg/Mg<sup>+2</sup> as  $E_f = E(\text{Mg}_x\text{Sn}) - [xE(\text{Mg}) + E(\text{Sn})]$  where  $x$  is the number of Mg atoms per Sn atoms,  $E(\text{Mg}_x\text{Sn})$  is the total energy per Sn atoms of Mg<sub>x</sub>Sn phase,  $E(\text{Mg})$  is the total energy per atom of Mg in hcp crystal lattice, and  $E(\text{Sn})$  is the total energy per atom of Sn in tetragonal crystal lattice. The optimized lattice parameters, formation energy per atom of all phases are summarized in Table 1. Our results for the crystalline phases are in excellent agreement with reported theoretical and experimental measurements.<sup>53-56</sup>

Obtaining intrinsic elastic properties of single crystal structures using DFT is well established in literature and is explained in length in our earlier works.<sup>46,47</sup> Briefly, when a uniform and infinitesimal strain is applied to a homogeneous system, the internal energy of the system can be expressed in terms of strain components. Using energy-strain curve, one can obtain the elastic constants for all phases. For instance in c-Mg<sub>2</sub>Sn with cubic symmetry, uniaxial distortion, volumetric distortion and pure shear were applied to obtain the three independent elastic constants i.e.  $C_{11}$ ,  $C_{12}$ , and  $C_{44}$ , respectively (Voigt notation is used for all elastic constants).<sup>63</sup> The isotropic nature of a-Mg<sub>2</sub>Sn phase only gives two independent elastic constants,  $C_{11}$  and  $C_{12}$  similarly obtainable through uniaxial and volumetric strains, respectively. For  $C_{11}$ , uniaxial strain was applied along three orthogonal directions and average  $C_{11}$  was determined. In a similar fashion, we obtained the five and six independent elastic constants of Mg and Sn crystal structures, respectively.

Moreover, crucial electrochemical properties were calculated including electrode potential  $-E_f/x$  with respect to Mg/Mg<sup>+2</sup>, and specific capacity  $nF/\Sigma M$ , where  $n$  is the total number of Mg electrons in the reaction,  $F$  is Faraday's constant (26.802 Ah/mol) and  $\Sigma M$  is the total molecular weight of Mg<sub>2</sub>Sn. We also obtained volumetric energy density versus a hypothetical 3.75 V cathode by a method introduced by Obrovac et al.<sup>64,65</sup>

## Results and Discussion

***Electrochemical Properties.*** The specific capacity of c/a-Mg<sub>2</sub>Sn phases as used in MIBs is 641 mAh g<sup>-1</sup> since both have the same total molecular weight and assuming the same number of Mg electrons participate in the reaction (it is noted that specific capacity in excess of 903 mAh g<sup>-1</sup> is also interchangeably reported in literature by taking into account only the molecular weight of Sn instead of Mg<sub>2</sub>Sn).<sup>31,34,36,37</sup> The volume expansion of the optimized a-Mg<sub>2</sub>Sn is about 160 % with reference to pure Sn, which is lower by 20 % when compared to c-Mg<sub>2</sub>Sn. We find the electrode potentials as low as 0.15 and 0.06 V for c, a-Mg<sub>2</sub>Sn, respectively. Comparative low potentials  $\approx$  0.04 V have been found for fully lithiated amorphous Si (a-Li<sub>3.75</sub>Si),<sup>66</sup> and fully lithiated amorphous C (a-Li<sub>0.75</sub>C<sub>6</sub>) in LIBs,<sup>67</sup> and have been reported experimentally for electrode materials in rechargeable batteries.<sup>66,68</sup> In Mg-Sn system, as obtained from our calculations, this gives a-Mg<sub>2</sub>Sn phase a volumetric energy density in excess of 8.50 Wh cc<sup>-1</sup> greater than 8.25 Wh cc<sup>-1</sup> for c-Mg<sub>2</sub>Sn.

***Examination of Amorphous Mg<sub>2</sub>Sn Phase.*** The optimized c-Mg<sub>2</sub>Sn and a-Mg<sub>2</sub>Sn phases are shown in Fig. 1a and b, respectively.<sup>69</sup> The former has a well-defined atomic positions, whereas the latter has a disordered atomic positions. RDFs results, as shown in Fig. 1c, further demonstrate that while c-Mg<sub>2</sub>Sn is characterized with well-defined peaks indicating the crystallinity of the phase, the peaks of a-Mg<sub>2</sub>Sn are flattened indicating the amorphousness of the phase, similar to amorphous Li-Si phase in Li-ion battery.<sup>70</sup> We also compare the amorphousness of a-Mg<sub>2</sub>Sn at the three chosen temperatures. Evidenced by the RDFs, we obtain qualitatively similar a-Mg<sub>2</sub>Sn phases regardless of the choice of annealing temperature.

The RDFs give us a qualitative understanding on the formation of a-Mg<sub>2</sub>Sn phase upon annealing. It fails to elaborate on the origin of amorphousness, and provide an atomic-level insight into interatomic bonds. We employ rings statistics technique as implemented in I.S.A.A.C.S. package to obtain such insight and compare it against c-Mg<sub>2</sub>Sn. The a-Mg<sub>2</sub>Sn phase—obtained by annealing at 2000 K—was chosen for further analyses as no significant

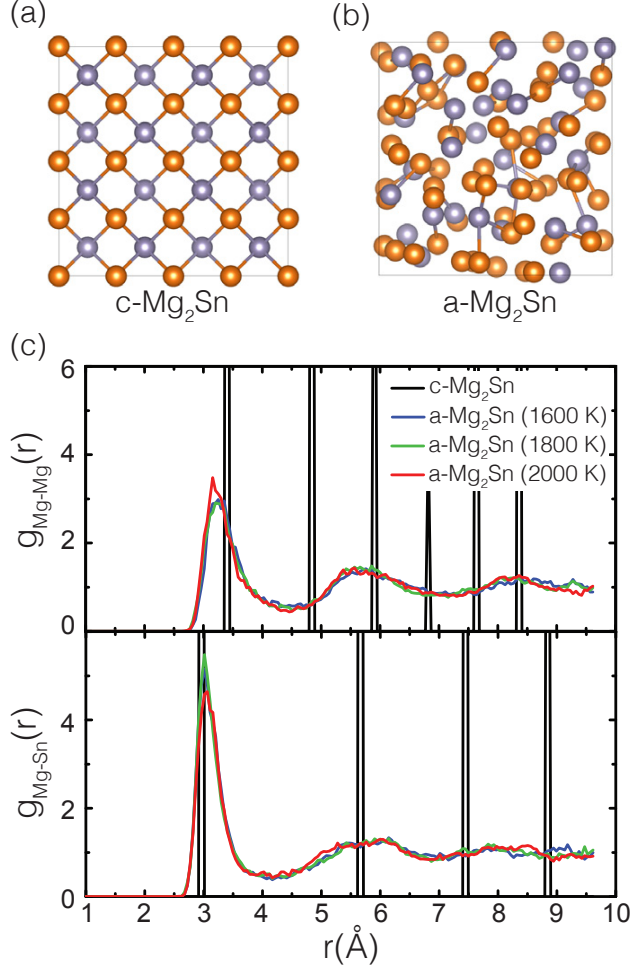


Figure 1. (a)  $c\text{-Mg}_2\text{Sn}$ , and (b)  $a\text{-Mg}_2\text{Sn}$  (obtained by annealing  $c\text{-Mg}_2\text{Sn}$  at 2000 K) super cells, (c) Radial distribution function  $g(r)$  for Mg-Mg and Mg-Sn in  $c\text{-Mg}_2\text{Sn}$ , and  $a\text{-Mg}_2\text{Sn}$  as obtained at three annealing temperatures. Orange and purple spheres denote Mg, and Sn atoms, respectively.

changes were found in results when other temperatures were used. The rings statistics results are shown in Fig. 2a. The abscissa shows different types of rings from 3–10 membered rings. The ordinate shows the number of rings per atom normalized by the total number of atoms in the unit cell. The cut-off distance of  $3.4 \text{ \AA}$ , and  $3.0 \text{ \AA}$  were chosen for Mg-Mg and Mg-Sn pairs, respectively, corresponding to the first peak in our RDF results (see Fig. 1a).

We have identified only 4-membered rings of Mg and Sn atoms in  $c\text{-Mg}_2\text{Sn}$  due to well-defined atomic positions in the crystalline structure representing a single sharp peak at four as shown in Fig. 2a (in black). The magnitude of 2 for the number of rings per atom for

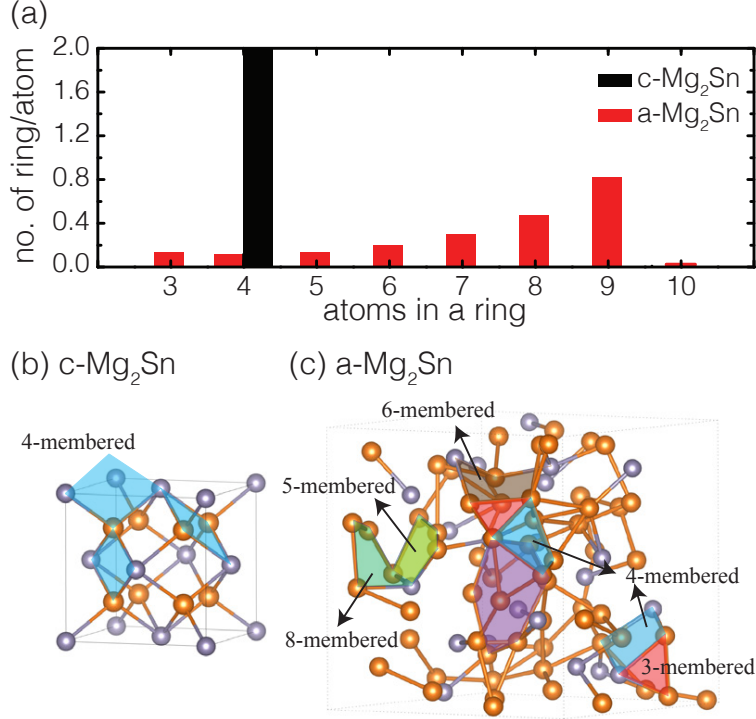


Figure 2. (a) Ring statistics for *c/a*-Mg<sub>2</sub>Sn phases, (b) Schematic representation of different rings in (b) *c*-Mg<sub>2</sub>Sn phase, (c) *a*-Mg<sub>2</sub>Sn phase. All single atoms which are not participating in any bonds were removed from the original *a*-Mg<sub>2</sub>Sn phase for visual clarity. Orange and purple spheres denote Mg, Sn atoms, respectively.

*c*-Mg<sub>2</sub>Sn is derived by a total number of the 4-membered rings, which is 12, normalized by six the total number of atoms in the unit cell. The 4-membered rings are schematically shown in Fig. 2b, constituting the *c*-Mg<sub>2</sub>Sn crystal structure. On the contrary, we see a disordered network of Mg and Sn atoms in *a*-Mg<sub>2</sub>Sn leading to the formation of series of 3- to-10-membered rings. The distribution of such rings is shown in Fig. 2a (in red). We have not seen any significant qualitative differences in ring statistic results when other *a*-Mg<sub>2</sub>Sn phases, obtained by different annealing temperatures, were used. The number of rings per atom falls within a narrow range of 0.4–0.8 with a relative dominance of 8, 9-membered rings. This disordered system characterized by existence of various rings—opposed to *c*-Mg<sub>2</sub>Sn—further signifies the formation of *a*-Mg<sub>2</sub>Sn phase. In order to provide an atomic-level view of *a*-Mg<sub>2</sub>Sn phase, a few multi-membered rings are identified and highlighted in Fig. 2c.

***Fundamental Elastic Behavior*** Table 2 outlines the second order elastic constants

Table 2: Second order elastic constants  $C_{ij}$ s (in GPa) of Mg, c-Mg<sub>2</sub>Sn, Sn, and a-Mg<sub>2</sub>Sn phases obtained from DFT calculations.

Phase	$C_{11}$	$C_{12}$	$C_{13}$	$C_{33}$	$C_{44}$	$C_{66}$
crystalline						
$\beta$ -Sn	72.22	33.55	30.59	87.77	19.66	23.71
Mg <sub>2</sub> Sn	76.02	23.41			31.97	
Mg	64.17	22.68	24.51	62.78	16.44	
crystalline (exp)						
$\beta$ -Sn	75.50	23.40	28.00	87.00	22.00	22.65
Mg <sub>2</sub> Sn	82.40	20.80			36.60	
Mg	59.74	26.24	21.70	61.70	16.39	
amorphous						
Mg <sub>2</sub> Sn	65.18	18.49				

$C_{ij}$ s of Mg, Sn and c/a-Mg<sub>2</sub>Sn phases as obtained from our DFT calculations. Our  $C_{ij}$ s are in good agreement with the experimental measurements and first principles calculations of elastic constants for crystalline Mg, Mg<sub>2</sub>Sn, Sn phases (see Table 2).<sup>53-56</sup> These values are elastic constants of single crystals as opposed to polycrystalline structures with randomly oriented single crystals and do not reflect the elastic properties of the microstructure of an alloys anode.<sup>50,71,72</sup> The correlation between the elastic properties of single crystals and an aggregate is made by employing the Voigt and Reuss continuum theories.<sup>73,74</sup> Moreover, Hill demonstrated that the arithmetic average of the Voigt and Reuss values gives a better approximations for the elastic properties of the polycrystalline microstructures. Table 3 presents the bulk moduli (B), Young’s moduli (E), and shear moduli (G) of polycrystalline Mg, c-Mg<sub>2</sub>Sn, Sn, and a-Mg<sub>2</sub>Sn adopting Hill averaging method. The  $B/G$  ratio, and anisotropy factor of Young’s and shear moduli (calculated as  $A_X = X_{max}/X_{min}$  with X being either Young’s or shear moduli) are also given in the table.<sup>75</sup> In addition, we plot Young’s and bulk moduli of all phases including a-Mg<sub>2</sub>Sn as a function of the Mg fraction  $y = x/(x + 1)$  in Fig. 3, where  $y= 0$  and  $1$  represents the pure polycrystalline Sn phase and Mg phase, respectively.

It is evident from Table 3 that Young’s and shear modulus for c-Mg<sub>2</sub>Sn are greater than that of pure Mg and Sn phases. This can be understood from  $B/G$  ratio—an indication to

Table 3: Bulk modulus (B), Young’s modulus (E) and shear modulus (G) of Mg, c-Mg<sub>2</sub>Sn,  $\beta$ -Sn, and a-Mg<sub>2</sub>Sn phases obtained via Hill (H) averaging methods from our DFT calculations. A<sub>E</sub> and A<sub>G</sub> are anisotropy of Young’s modulus, shear modulus, respectively. All moduli are in GPa.

Phase	B <sub>H</sub>	E <sub>H</sub>	G <sub>H</sub>	B <sub>H</sub> / G <sub>H</sub>	A <sub>E</sub>	A <sub>G</sub>
crystalline						
$\beta$ -Sn	46.74	56.13	21.59	2.17	1.36	1.32
Mg <sub>2</sub> Sn	40.95	71.5	29.57	1.38	1.17	1.21
Mg	37.17	47.78	18.58	2.09	1.14	1.26
amorphous						
Mg <sub>2</sub> Sn	34.05	57.01	23.35	1.46	1	1

the ductility of metal alloys suggested by Pugh.<sup>76</sup> The ratio less(greater) than 1.75 suggests a brittle(ductile) behavior.<sup>76</sup> Pure Mg and Sn phases are thus ductile materials, while c-Mg<sub>2</sub>Sn is more brittle. The transition from ductile (Sn) to brittle (c-Mg<sub>2</sub>Sn) upon Sn magnesiation could be a responsible factor for a sudden increase in moduli. This elastic behavior may lead to the accumulation of internal stresses causing particle cracking and fracture during discontinuous phase transformation upon magnesiation/de-magnesiation during the formation of c-Mg<sub>2</sub>Sn phase.<sup>36</sup> This phenomenon is distinct from the mechanical response of group-14,15 elements to sodiation and Li-Si alloy anodes but somewhat similar to Li-Sn system (in which Sn lithiation also experiences a sudden increase in Young’s and shear moduli with respect to pure Sn phase).<sup>43-47</sup> There is one remarkable difference: Sn magnesiation is susceptible to electrochemically driven amorphization. Our results demonstrate that a-Mg<sub>2</sub>Sn has become elastically soft by  $\approx 20\%$  with respect to c-Mg<sub>2</sub>Sn. This elastic softening makes the moduli’s trend to follow an approximate linear dependence on the Mg fraction as opposed to c-Mg<sub>2</sub>Sn (see Fig. 3). This behavior may suggest a more gradual magnesiation-induced phase transformation in favor of easing the build-up of severe internal stresses. We further see that all crystalline phases are rather elastically isotropic polycrystalline materials due to low anisotropy values consistent with the small deviation of their bulk and shear moduli from the linear dependency (see Table 3, where A =1, A >1 signifies isotropic and anisotropic

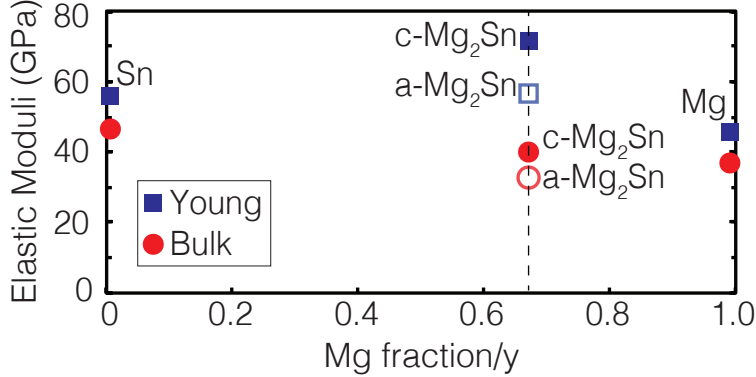


Figure 3. Concentration-dependent Elastic Moduli: Young’s modulus ( $E_H$ ) and bulk modulus ( $B_H$ ) of  $Mg_xSn$  alloys as a function of Mg fraction  $y = x/(x + 1)$ .

behavior, respectively).

**Atomic-scale Insights via Charge Analysis.** We obtain the net charges on each atom by employing Bader charge population analysis using electronic charge distribution from our DFT calculations.<sup>77</sup> Table 4 presents the calculated charges. In c-Mg<sub>2</sub>Sn phase, Mg and Sn atoms are in a single specific charge state. Mg atom donates majority of its divalent electrons. Each Sn atom is surrounded by two Mg atoms hence adopting double Mg charge state (positive sign). On the contrary, in a-Mg<sub>2</sub>Sn, atoms are in various charge states—implying an inhomogeneous charge distribution—due to the participation of Mg and Sn atoms in complex bonding networks. While it is evident that the charge state of Mg atoms falls in a wide range for a-Mg<sub>2</sub>Sn phase (see Table 4), average charge remains nearly at  $-1.1 \bar{e}$ . This together with the inhomogeneity nature of net charges is another indication to the amorphousity of a-Mg<sub>2</sub>Sn phase along with our RDFs and ring statistics results, and supports the existence of local Mg-Sn networks. The calculations further suggest that the average number of Mg-Sn bonds is decreased by going from c-Mg<sub>2</sub>Sn to a-Mg<sub>2</sub>Sn further supporting the realized elastic softening behavior.

Table 4: Net charges on Mg and Sn atoms in c/a-Mg<sub>2</sub>Sn phases obtained using Bader charge population analysis.

Phase	Net charge on	
	Mg atoms	Sn atoms
c-Mg <sub>2</sub> Sn	-1.43	2.85
a-Mg <sub>2</sub> Sn	-0.32 to -1.32	1.12 to 2.83

## Conclusions

In summary, we obtained the fundamental electrochemical and elastic properties of c/a-Mg<sub>2</sub>Sn alloy anodes for Mg-ion batteries. We created the a-Mg<sub>2</sub>Sn phase using annealing-quenching technique, and examined its amorphousity through RDFs and ring statistics. We found while the elastic moduli of c-Mg<sub>2</sub>Sn phase show an abrupt increase (as large as 27 %) with respect to pure Sn, a-Mg<sub>2</sub>Sn is elastically softened by 20 % with respect to c-Mg<sub>2</sub>Sn and follows a linear trend of moduli in binary Mg-Sn system. The elastic softening is attributed to the formation of various complex rings resulted in uneven charge distributions. We believe that the electrochemically-induced failures during Sn $\leftrightarrow$ c-Mg<sub>2</sub>Sn phase transformation could be due to the development of incompatible strains and stresses and subsequent sudden change in elastic moduli. This study suggests that the formation of a-Mg<sub>2</sub>Sn phase could be the key to mitigate this problem. The Sn $\leftrightarrow$ a-Mg<sub>2</sub>Sn undergoes a relatively more gradual phase transformation which increases the likelihood of alleviating the build-up of internal stresses and capacity fade during volume change. Our results serve as the first step towards the development of failure-free Mg-Sn alloy anode suitable for the next generation of Mg-ion batteries. They can essentially be used in constructing macroscopic models to better understand deformation behaviors, magnesianion-induced amorphization, and different modes of failures.

## Acknowledgement

MM, ES, and NM gratefully acknowledge computational support from Monash University Campus Cluster, Pawsey Supercomputing Facility and the National Computing Infrastructure funded by the Australian Government.

## References

- (1) Nitta, N.; Wu, F.; Lee, J. T.; Yushin, G. *Materials today* **2015**, *18*, 252–264.
- (2) Vaalma, C.; Buchholz, D.; Weil, M.; Passerini, S. *Nature Reviews Materials* **2018**, *3*, 18013.
- (3) Opitz, A.; Badami, P.; Shen, L.; Vignarooban, K.; Kannan, A. *Renewable and Sustainable Energy Reviews* **2017**, *68*, 685–692.
- (4) Peters, J. F.; Baumann, M.; Zimmermann, B.; Braun, J.; Weil, M. *Renewable and Sustainable Energy Reviews* **2017**, *67*, 491–506.
- (5) Muñoz-Márquez, M. Á.; Saurel, D.; Gómez-Cámer, J. L.; Casas-Cabanas, M.; Castillo-Martínez, E.; Rojo, T. *Advanced Energy Materials* **2017**, *7*, 1700463.
- (6) Luo, W.; Shen, F.; Bommier, C.; Zhu, H.; Ji, X.; Hu, L. *Accounts of chemical research* **2016**, *49*, 231–240.
- (7) Ellis, B. L.; Nazar, L. F. *Current Opinion in Solid State and Materials Science* **2012**, *16*, 168–177.
- (8) Bauer, A.; Song, J.; Vail, S.; Pan, W.; Barker, J.; Lu, Y. *Advanced Energy Materials* **2018**, 1702869.
- (9) Noorden, R. *Nature* **2014**, *507*, 26–28.

- (10) Massé, R. C.; Uchaker, E.; Cao, G. *Science China Materials* **2015**, *58*, 715–766.
- (11) Kubota, K.; Dahbi, M.; Hosaka, T.; Kumakura, S.; Komaba, S. *The Chemical Record* **2018**, *18*, 459–479.
- (12) Huang, Y.; Zheng, Y.; Li, X.; Adams, F.; Luo, W.; Huang, Y.; Hu, L. *ACS Energy Letters* **0**, *0*, null.
- (13) Yoo, H. D.; Shterenberg, I.; Gofer, Y.; Gershinsky, G.; Pour, N.; Aurbach, D. *Energy & Environmental Science* **2013**, *6*, 2265–2279.
- (14) Saha, P.; Datta, M. K.; Velikokhatnyi, O. I.; Manivannan, A.; Alman, D.; Kumta, P. N. *Progress in Materials Science* **2014**, *66*, 1–86.
- (15) Choi, J. W.; Aurbach, D. *Nature Reviews Materials* **2016**, *1*, 16013.
- (16) Levi, E.; Gofer, Y.; Aurbach, D. *Chemistry of Materials* **2009**, *22*, 860–868.
- (17) Muldoon, J.; Bucur, C. B.; Oliver, A. G.; Sugimoto, T.; Matsui, M.; Kim, H. S.; Allred, G. D.; Zajicek, J.; Kotani, Y. *Energy & Environmental Science* **2012**, *5*, 5941–5950.
- (18) Sun, X.; Bonnicksen, P.; Nazar, L. F. *ACS Energy Letters* **2016**, *1*, 297–301.
- (19) Tutusaus, O.; Mohtadi, R.; Singh, N.; Arthur, T. S.; Mizuno, F. *ACS Energy Letters* **2016**, *2*, 224–229.
- (20) Luo, J.; He, S.; Liu, T. L. *ACS Energy Letters* **2017**, *2*, 1197–1202.
- (21) Matsui, M. *Journal of Power Sources* **2011**, *196*, 7048–7055.
- (22) Banerjee, S.; Pati, S. K. *Chemical Communications* **2016**, *52*, 8381–8384.
- (23) Schloffer, D.; Bozorgi, S.; Sherstnev, P.; Lenardt, C.; Gollas, B. *Journal of Power Sources* **2017**, *367*, 138–144.

- (24) Bucur, C. B. *Challenges of a Rechargeable Magnesium Battery: A Guide to the Viability of this Post Lithium-Ion Battery*; Springer International Publishing: Cham, 2018; pp 39–53.
- (25) Niu, J.; Gao, H.; Ma, W.; Luo, F.; Yin, K.; Peng, Z.; Zhang, Z. *Energy Storage Materials* **2018**, *196*, 351–360.
- (26) Arthur, T. S.; Singh, N.; Matsui, M. *Electrochemistry Communications* **2012**, *16*, 103–106.
- (27) Malyi, O. I.; Tan, T. L.; Manzhos, S. *Journal of Power Sources* **2013**, *233*, 341–345.
- (28) Singh, N.; Arthur, T. S.; Ling, C.; Matsui, M.; Mizuno, F. *Chemical communications* **2013**, *49*, 149–151.
- (29) Shao, Y.; Gu, M.; Li, X.; Nie, Z.; Zuo, P.; Li, G.; Liu, T.; Xiao, J.; Cheng, Y.; Wang, C. *Nano letters* **2013**, *14*, 255–260.
- (30) Periyapperuma, K.; Tran, T. T.; Purcell, M.; Obrovac, M. *Electrochimica Acta* **2015**, *165*, 162–165.
- (31) Parent, L. R.; Cheng, Y.; Sushko, P. V.; Shao, Y.; Liu, J.; Wang, C.-M.; Browning, N. D. *Nano letters* **2015**, *15*, 1177–1182.
- (32) Tan, Y.-H.; Yao, W.-T.; Zhang, T.; Ma, T.; Lu, L.-L.; Zhou, F.; Yao, H.-B.; Yu, S.-H. *ACS nano* **2018**,
- (33) Murgia, F.; Laurencin, D.; Weldekidan, E. T.; Stievano, L.; Monconduit, L.; Doublet, M.-L.; Berthelot, R. *Electrochimica Acta* **2018**, *259*, 276–283.
- (34) Yaghoobnejad Asl, H.; Fu, J.; Kumar, H.; Welborn, S. S.; Shenoy, V. B.; Detsi, E. *Chemistry of Materials* **2018**, *5*, 1815–1824.

- (35) Wang, Z.; Su, Q.; Shi, J.; Deng, H.; Yin, G.; Guan, J.; Wu, M.; Zhou, Y.; Lou, H.; Fu, Y. Q. *ACS applied materials & interfaces* **2014**, *6*, 6786–6789.
- (36) Nguyen, D.-T.; Song, S.-W. *Journal of Power Sources* **2017**, *368*, 11–17.
- (37) Huang, B.; Pan, Z.; Su, X.; An, L. *Journal of Power Sources* **2018**, *395*, 41–59.
- (38) Jin, W.; Li, Z.; Wang, Z.; Fu, Y. Q. *Materials Chemistry and Physics* **2016**, *182*, 167–172.
- (39) Obrovac, M.; Christensen, L. *Electrochemical and Solid-State Letters* **2004**, *7*, A93–A96.
- (40) Kasavajjula, U.; Wang, C.; Appleby, A. *J. Power Sources* **2007**, *163*, 1003–1039.
- (41) Zhang, W. *J. Power Sources* **2011**, *196*, 13–24.
- (42) Kreder III, K. J.; Heligman, B. T.; Manthiram, A. *ACS Energy Letters* **2017**, *2*, 2422–2423.
- (43) Shenoy, V.; Johari, P.; Qi, Y. *J. Power Sources* **2010**, *195*, 6825–6830.
- (44) Park, C.-M.; Kim, J.-H.; Kim, H.; Sohn, H.-J. *Chemical Society Reviews* **2010**, *39*, 3115–3141.
- (45) Stournara, M.; Guduru, P.; Shenoy, V. *J. Power Sources* **2012**, *208*, 165–169.
- (46) Mortazavi, M.; Deng, J.; Shenoy, V. B.; Medhekar, N. V. *Journal of Power Sources* **2013**, *225*, 207–214.
- (47) Mortazavi, M.; Ye, Q.; Birbilis, N.; Medhekar, N. V. *Journal of Power Sources* **2015**, *285*, 29–36.
- (48) Grosch, G. H.; Range, K.-J. *Journal of alloys and compounds* **1996**, *235*, 250–255.
- (49) Hardie, D.; Parkins, R. *Philosophical Magazine* **1959**, *4*, 815–825.

- (50) Chen, J.; Bull, S.; Roy, S.; Mukaibo, H.; Nara, H.; Momma, T.; Osaka, T.; Shacham-Diamand, Y. *J. Phys. D: Appl. Phys.* **2008**, *41*, 025302.
- (51) Mukaibo, H.; Momma, T.; Shacham-Diamand, Y.; Osaka, T.; Kodaira, M. *Electrochem. Solid-State Lett.* **2007**, *10*, A70.
- (52) Sen, R.; Johari, P. *ACS applied materials & interfaces* **2017**, *9*, 40197–40206.
- (53) Davis, L.; Whitten, W.; Danielson, G. *Journal of Physics and Chemistry of Solids* **1967**, *28*, 439–447.
- (54) Ganeshan, S.; Shang, S.; Zhang, H.; Wang, Y.; Mantina, M.; Liu, Z. *Intermetallics* **2009**, *17*, 313–318.
- (55) Zhou, D.; Liu, J.; Xu, S.; Peng, P. *Computational Materials Science* **2012**, *51*, 409–414.
- (56) Liu, Y.; Hu, W.-C.; Li, D.-J.; Zeng, X.-Q.; Xu, C.-S. *Physica Scripta* **2013**, *88*, 045302.
- (57) Kresse, G.; Furthmüller, J. *Phys. Rev. B* **1996**, *54*, 11169.
- (58) Kresse, G.; Joubert, D. *Phys. Rev. B* **1999**, *59*, 1758.
- (59) Blöchl, P. *Phys. Rev. B* **1994**, *50*, 17953.
- (60) Pearson, W. *Vols. I and II (Pergamon Press, Oxford, 1964, 1967)* **1958**,
- (61) Monkhorst, H.; Pack, J. *Phys. Rev. B* **1976**, *13*, 5188–5192.
- (62) Le Roux, S.; Petkov, V. *Journal of Applied Crystallography* **2010**, *43*, 181–185.
- (63) Landau, L.; Lifshitz, E. *Theory of Elasticity 3rd Ed.*; Butterworth-Heinemann, Oxford, UK, 1986.
- (64) Obrovac, M.; Christensen, L.; Le, D. B.; Dahn, J. R. *Journal of The Electrochemical Society* **2007**, *154*, A849–A855.

- (65) Obrovac, M.; Chevrier, V. *Chemical reviews* **2014**, *114*, 11444–11502.
- (66) Li, J.; Dahn, J. *Journal of The Electrochemical Society* **2007**, *154*, A156–A161.
- (67) Stournara, M. E.; Qi, Y.; Shenoy, V. B. *Nano letters* **2014**, *14*, 2140–2149.
- (68) Pharr, M.; Suo, Z.; Vlassak, J. J. *Nano letters* **2013**, *13*, 5570–5577.
- (69) Momma, K.; Izumi, F. *Journal of applied crystallography* **2011**, *44*, 1272–1276.
- (70) Chevrier, V.; Dahn, J. R. *Journal of the Electrochemical Society* **2009**, *156*, A454–A458.
- (71) Sethuraman, V. A.; Chon, M. J.; Shimshak, M.; Van Winkle, N.; Guduru, P. R. *Electrochemistry Communications* **2010**, *12*, 1614–1617.
- (72) Sethuraman, V.; Chon, M.; Shimshak, M.; Srinivasan, V.; Guduru, P. *J. Power Sources* **2010**, *195*, 5062–5066.
- (73) Voigt, W. *Lehrbuch der Kristallphysik*, Teubner, Leipzig. 1928.
- (74) Reuss, A. *ZAMM-Journal of Applied Mathematics and Mechanics* **1929**, *9*, 49–58.
- (75) Ranganathan, S.; Ostoja-Starzewski, M. *Phys. Rev. Lett.* **2008**, *101*, 55504.
- (76) Pugh, S. *Philos. Mag.* **1954**, *45*, 823–843.
- (77) Bader, R. *Atoms in Molecules: A Quantum Theory*; Int Monogr Chem; Oxford University Press, 1990.

# Graphical TOC Entry

